Journal of Materials Chemistry A

Accepted Manuscript

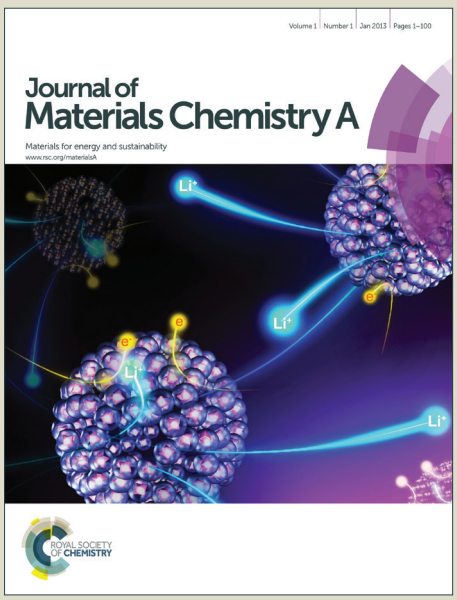

ROYAL SOCIETY OF CHEMISTRY

www.rsc.org/materialsA

Journal of Materials Chemistry A RSCPublishing

COMMUNICATION

An Investigation on Morphology Effect in Fe_2O_3 Anodes for Lithium Ion Batteries†

Cite this: DOI: 10.1039/xoxxoooooox

Hao Liu*[a] and Guoxiu Wang*[a]

Received ooth January 2014,
Accepted ooth January 2014

DOI: 10.1039/xoxxoooooox

www.rsc.org/

Morphology control strategies have been widely used to boost the tolerance of anode materials against dramatic volume change during charge/discharge processes. Herein, we found solid scientific evidence demonstrating that electrochemical properties of cavity contained materials are superior to their solid counterparts.

Due to its high energy density compared to conventional rechargeable batteries, the lithium ion battery dominates the market of portable devices and is considered as one of the most promising battery options for electric vehicles (EVs).[1] However, present-daymicro-size electrode materials can only operate at low currents and may cause polarization and pulverization while operating at high currents.[2] Thus, it is critical that new electrode materials with enhanced electrochemical performance for EVs are developed. Nanomaterials have attracted great attention for use in lithium ion batteries, as their low dimensions provide shorter pathways for fast lithium ion migration; therefore, achieve high power for EVs.

However, no matter how advanced the design for nanomaterials, it is inevitable that electrode materials will suffer from volume change during charge/discharge processes, due to the volume expansion/shrinkage caused by intercalation/de-intercalation of lithium ions. To alleviate the stress of electrode materials during charge/discharge, many attempts have been made in preparing novel structured materials with void buffer spaces, including mesoporous, hollow spherical and yolk-shell structured materials.[3-7] Bruce *et al.* developed a series of ordered mesoporous structured materials for lithium ion batteries.[3] The internal mesopores of 2 - 50 nm can be flooded with electrolyte, ensuring a high surface area of electrolyte/electrode interphase, and hence a high flux of lithium across the interface. Compared with the random porosity between the nanoparticles, the ordered mesoporous structure ensures that this is an even distribution of electrolyte in contact with the electrode surface and a uniform buffer space for electrode expansion. Meanwhile, several of ordered mesoporous structured electrode materials were widely investigated by other research groups.[4] Lou *et al.* have devoted to hollow structured electrode materials for lithium ion batteries.[5] The hollow structures (spheres, boxes, core-shell *etc*) with high surface area and different shell morphologies (*e.g.* nanopolycrystals, nanosheets) can provide efficient active sites and short pathways for lithium ion migration. Moreover, the hollow inner cavity can buffer the volume change during charge/discharge. Recently, a yolk-shell structure has received much interest because of its unique core-shell structure and void space between core and shell, which may be applied to applications such as nanoreactors, energy storage and drug delivery.[6] Cui *et al.* recently reported a novel yolk-shell structured sulphur-TiO_2 composite, by partially dissolving sulphur in S-TiO_2 core-shell particles.[7] The yolk-shell composite accommodates the volumetric expansion of sulphur in the void space, and presents a high specific capacity and excellent long term performance for lithium-sulphur batteries.

The above mentioned reports reveal an electrochemical performance of electrode materials by raising a hypothesis of volumetric expansion depression. However, none of them provide systemic scientific evidence to explain the enhancement, especially in respect to electrochemistry. To investigate the morphology effect of void space in materials, herein, we prepared two groups of Fe_2O_3 materials with/without cavity, nanorods vs. nanotubes and nanodisks vs. nanorings, and measured the electrochemical performances as anode materials for lithium ion batteries. Furthermore, activation energy of as-prepared materials can be obtained by electrochemical impedance spectroscopy (EIS) method, giving instructive comparison in each group.

Nanostructured Fe_2O_3 materials were prepared by a facile hydrothermal method (experimental details in supporting information). Figure 1 shows the scanning electron microscopy (SEM) images of nanostructured Fe_2O_3 materials, which demonstrate the morphologies of as-prepared materials (nanorods, nanotubes, nanodisks and nanorings). Figure 1(a) presents the SEM image of Fe_2O_3 nanorods, illustrating a large scale of spindle-like nanorods with lengths of about 1 micron and widest diameters of around 150 - 200 nm. Figure 1(b) shows the SEM image of Fe_2O_3 nanotubes, demonstrating the similar size in length and diameter to nanorods as shown in Figure 1(a). The high resolution SEM image as shown in the inset of Figure 1(b) clearly presents the open-end tip, implying a tubular structure. Figure 1(c) shows the SEM image of Fe_2O_3 nanodisks obtained in a higher concentration of $H_2PO_4^-$ solvent,

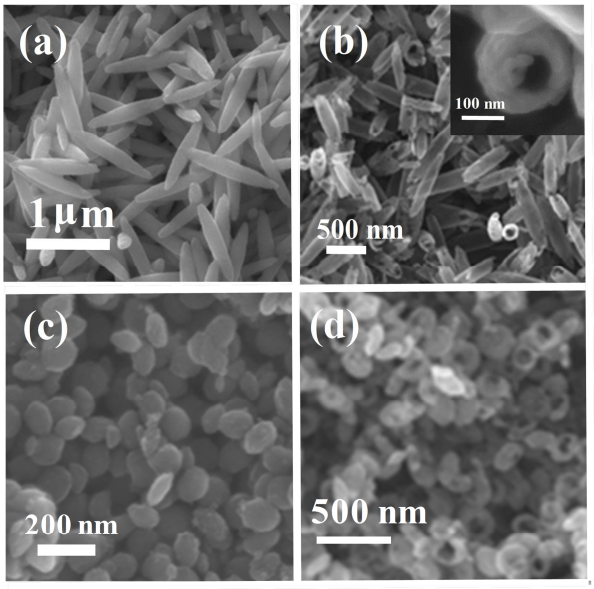

Figure 1. SEM images of (a) nanorods, (b) nanotubes, (c) nanodisks and (d) nanorings Fe_2O_3 materials.

demonstrating a large scale convex-disk-like morphology. The Figure 1(d) presents the SEM image of Fe_2O_3 nanorings, illustrating a similar size to the nanodisks of about 100 nm in diameter.

The microstructure of Fe_2O_3 nanomaterials were examined by transmission electron microscopy (TEM). The TEM image as shown in Figure 2(a) confirms the solid structure morphology of nanorods. The high resolution image in Figure 2(b) implies the fringe structure of Fe_2O_3 nanorods at the location of white cross point as denoted in Figure 2(a). The interplanar distances of 0.27 and 0.37 nm as shown in Figure 2(b) are consistent with the standard d-spacing of (104) and (012) planes of Fe_2O_3. The TEM image in Figure 2(c) clearly shows the inner hollow structure of Fe_2O_3 nanotubes. The HRTEM image in Figure 2(d) confirms the crystal structure of alpha-phase Fe_2O_3 nanotubes. Figure 2(e) shows the TEM image of Fe_2O_3 nanodisks, demonstrating convex-disk-like structure with a diameter of about 100 nm. The HRTEM image in Figure 2(f) demonstrates the lattice structure of nanodisks, which presents the view perpendicular to the [012] direction. The Figure 2(g) shows the TEM images of Fe_2O_3 nanorings with typical ring-like structure. The HRTEM of Fe_2O_3 nanorings as shown in Figure 2(h) implies the polycrystalline structure of nanorings, with the exposed [012] directions at random.

The SEM and TEM observations clearly indicate that the target materials, two groups of Fe_2O_3 materials with/without cavity, nanorods vs. nanotubes and nanodisks vs. nanorings, were successfully prepared. The growth mechanism of Fe_2O_3 nanostructures has been raised by some research group.[8] The $H_2PO_4^-$ concentration also plays an important role in affecting the morphology of Fe_2O_3 nanoparticles. At lower concentration, the nanoparticles grow along the preferential [001] direction. In a higher concentration solvent, the denser $H_2PO_4^-$ will block the growth along the preferential direction, so that the size of product is smaller than that of product from lower $H_2PO_4^-$ solvent (eg. nanodisks vs. nanorods). It is noticed that the diameters of materials in each group are similar, and the inner cavity can be produced by prolonging the reaction period. This implies an etching process by the existence of $H_2PO_4^-$ in the solvent. With the hydrolysis of Fe^{3+}, the concentrations of H^+ will be increased. Newly produced H^+ will collaborate with $H_2PO_4^-$ etch the formed Fe_2O_3 from highest Fe^{3+} exposed (100) facet.

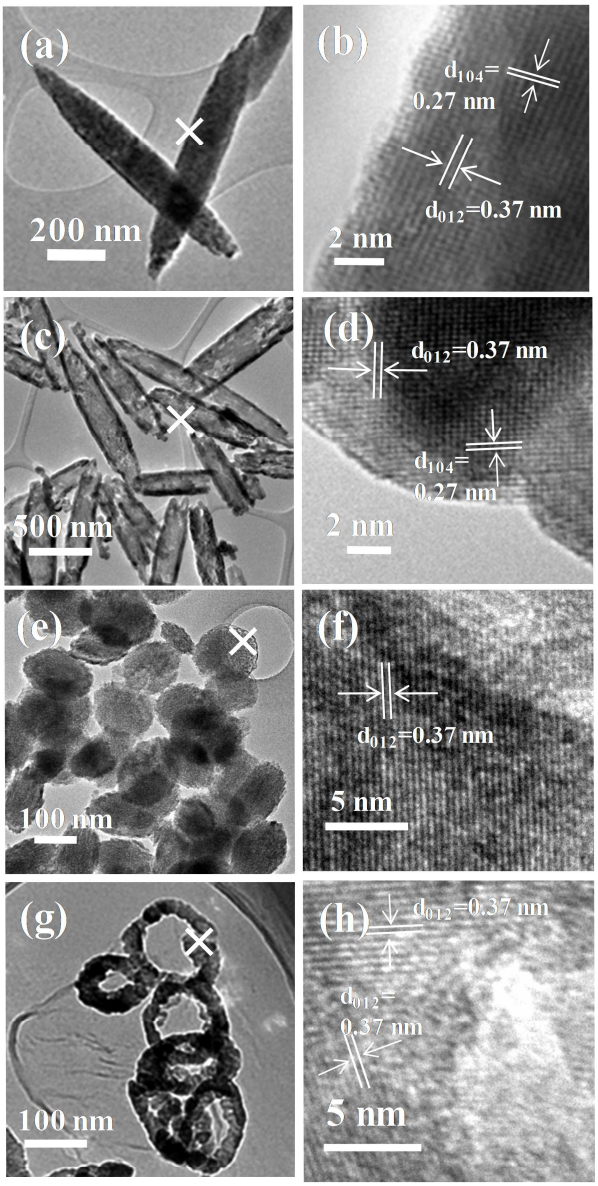

Figure 2. TEM images of (a) nanorods, (c) nanotubes, (e) nanodisks and (g) nanorings Fe_2O_3 materials; and HRTEM images in (c), (f), (i) and (l), corresponding to the areas denoted as white crosses in (b), (d), (f) and (h), respectively.

As a result, the dissolution process continuously proceeded along the [001] direction to form the hollow structure (tubes or rings).

The X-ray diffraction patterns of nano-structured Fe_2O_3 materials are shown in Figure S1. The Fe_2O_3 nanorods and nanotubes show pure rhombohedral hematite structure (JCPDS No. 33-0664). For the Fe_2O_3 nanodisks and nanorings, minor impurity exists in both products, which can be indexed to the $Fe_4(PO_4)_3(OH)_3$ (JCPDS 42-0429), the same as the published literature.[8] This is owing to the higher concentration of $H_2PO_4^-$ anion in reactant for the formation of nanodisks and nanorings than that of nanorods and nanotubes. The nitrogen sorption isotherms and corresponding pore size distributions of Fe_2O_3 products are shown in Figure S2. The specific surface area of Fe_2O_3 nanorods, nanotubes, nanodisks and nanorings are 42.4, 68.4, 52.1 and 89.6 m^2g^{-1}, respectively, as summarized in Table S2, calculated by the Brunauer-Emmett-Teller

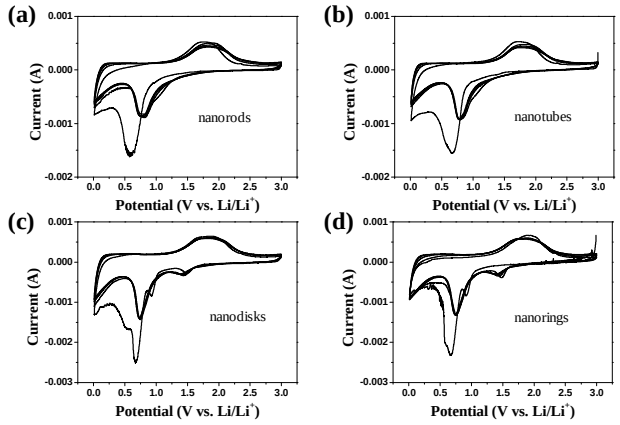

Figure 3. Cyclic voltammetry (CV) curves of nanorods, nanotubes, nanodisks and nanorings Fe_2O_3 electrode materials carried out between 0.01 and 3 V at scanning rate of 0.1mV/s, for first 5 cycles.

(BET) method. The surface area of Fe_2O_3 nanotubes and nanorings are much higher than their solid counterparts (nanorods and nanodisks), which can be ascribed to the lower dimensional size of polycrystals. The pore size distributions of the Fe_2O_3 materials calculated from the Barret-Joyner-Halenda (BJH) method are shown as insets of Figure 2(b), indicating that the as-prepared Fe_2O_3 materials are highly uniform with pore sizes between 2.2 and 2.5 nm (summarized in Table S2) which is attributed to the void space between polycrystals.

Cyclic voltammetry (CV) measurements of nanorods, nanotubes, nanodisks and nanorings Fe_2O_3 materials were carried out to investigate the diffusion of lithium ions in the solid state of electrode materials, as shown in Figure 3. The CV curves of Fe_2O_3 nanorods and nanotubes are the typical shape of alpha phase hematite material, which is similar to previous reports.[9] For instance, in Figure 3 (a), the board peak that appeared at about 0.61 V in the cathodic process in the first scanning cycle could be contributed to the reduction reaction from Fe^{3+} to Fe^0. In addition, this cathodic process is also associated with electrolyte decomposition to form the solid electrolyte interphase (SEI) layer and the reversible conversion reaction of lithium ion intercalation to form Li_2O. An anodic peak is present at about 1.80 V, corresponding to the reversible oxidation of Fe^0 to Fe^{3+}. In the subsequent cycles, the cathodic peak potential shifts to 0.78 V. The CV curves of the Fe_2O_3 nanorods and nanotubes electrode are identical from the second cycles, indicating high reversibility and good capacity retention at a low scanning rate (0.1 mV s^{-1}). For the CV curves of Fe_2O_3 nanodisks and nanorings electrodes, as shown in Figures 3 (c) and (d), both present an additional cathodic peak in each cycle. In the first cycle, the additional cathodic peak appears at around 1.0 V, which can be attributed to the reduction of Fe^{3+} in the phosphate complex. Because of the weaker coordination force between Fe^{3+} and $(PO_4)^{3-}$ polyanion than that between Fe^{3+} and O^{2-}, the Fe^{3+} species chelated with $(PO_4)^{3-}$ was preferentially reduced. In the following cycles, this peak shifts to about 1.5 V. This additional reduction peak to the typical CV curve of Fe_2O_3 reconfirms the existence of impurity in Fe_2O_3 nanodisks and nanorings, which is coincident with the XRD results. The CV curves of Fe_2O_3 nanodisks and nanorings electrodes also demonstrate excellent reversibility of these electrodes, according to the good superposition of CV curves in subsequent cycles.

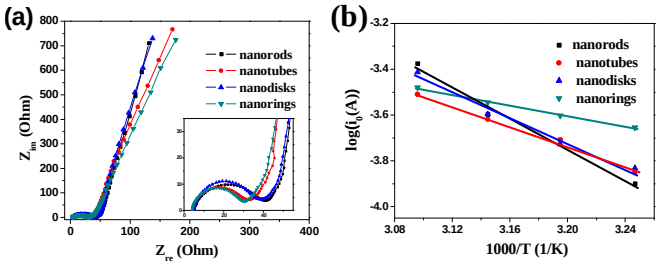

Figure 4. (a) Nyquist plots of nanorods, nanotubes, nanodisks and nanorings Fe_2O_3 electrode materials tested at room temperature. (b) Arrhenius plots of log i_0 versus 1/T for the fresh electrodes of nanorods, nanotubes, nanodisks and nanorings Fe_2O_3 collected at 2 V, in different temperatures of 35, 40, 45, 50 ℃.

Figure 4 (a) shows Nyquist plots of nanorods, nanotubes, nanodisks and nanorings Fe_2O_3 electrode materials tested at room temperature, which were measured by electrochemical impedance spectroscopy (EIS) method. All profiles exhibit a semicircle in the moderate frequency region and a straight line in the low frequency region. For each profile, the straight line in the low frequency region implies a typical Warburg behaviour, which is related to the diffusion of lithium ions in the solid state of electrode materials. The depressed semicircle in the moderate frequency region is attributed to the charge transfer process. The numerical value of the diameter of the semicircle on the Z_{re} axis gives an approximate indication of the charge transfer resistance (R_{ct}). In the enlarged inset figure of Figure 2(a), it is apparent that the charge transfer resistance of electrode materials with cavity, namely, nanotubes and nanorings, are much lower than those of the solid counterparts (nanorods and nanodisks).

For lithium ions intercalation reaction, the apparent activation energy (E_a), namely, the energy barrier between reactant and product, interprets different value for each material. The E_a for lithium intercalation and exchange current (i_0) can be calculated from the equation.[10]

$$i_0 = RT/(nFR_{ct}) = A\exp(-E_a/RT)$$

where R is the gas constant, T is the absolute temperature, n is the number of transferred electrons, F is the Faraday constant, R_{ct} is the charge transfer resistance, and A is a temperature-independent coefficient. The electrochemical impedance spectra tested at different temperatures of 35, 40, 45, 50 ℃ and their Arrhenius plots of log i_0 versus the reciprocal of absolute temperature (1/T) are summarized in Figure 4 (b). The activation energies are 65.09, 42.19, 52.76 and 22.19 kJ mol^{-1} for Fe_2O_3 nanorods, nanotubes, nanodisks and nanorings, respectively, calculated by the above mentioned equations. Interestingly, the activation energies of Fe_2O_3 materials with a hollow cavity are lower than their counterparts. The lower activation energy of Fe_2O_3 nanotubes and nanorings, as well as their lower charge transfer resistances, can be attributed to the facile charge transfer and lithium diffusion dynamics at the lower dimensional size in Fe_2O_3 nanotubes and nanorings, as they provided a higher surface area and shorter pathway for lithium ion diffusion, compared with their counterparts. This reduction of the charge transfer resistances and activation energies are beneficial in improving charge and electron kinetics in the electrode materials, and hence, enhance the electrochemical performance for lithium storage.

The galvanostatic charge/discharge measurements of nanorods, nanotubes, nanodisks and nanorings Fe_2O_3 electrode materials were carried out at testing currents of 0.1, 1 and 10 A g^{-1} (approximate to

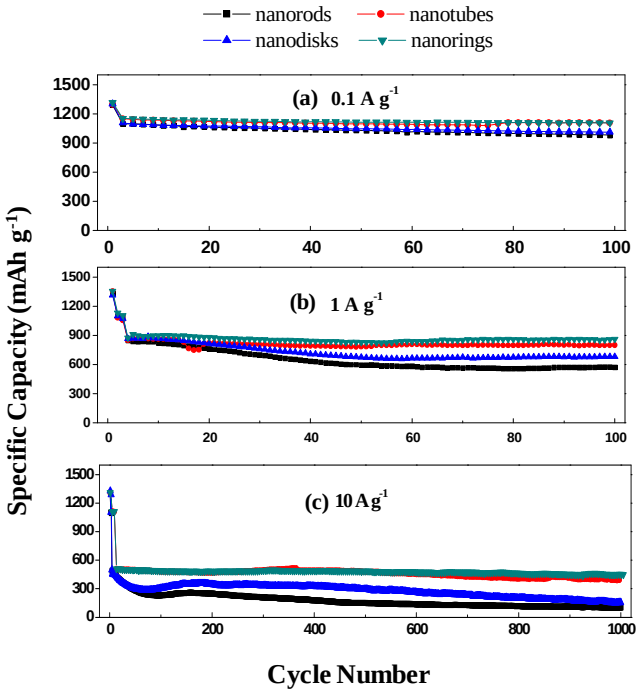

Figure 5. Electrochemical performance of nanorods, nanotubes, nanodisks and nanorings Fe_2O_3 electrode materials at testing currents of 0.1, 1 and 10 A g^{-1} (approximate to 0.1, 1 and 10 C) for 100, 100 and 1000 cycles.

0.1, 1 and 10 C) for 100, 100 and 1000 cycles, as shown in Figure 5. At low current charge/discharge testing (0.1C), the initial specific discharge capacities of nanorods, nanotubes, nanodisks and nanorings Fe_2O_3 electrode materials are 1291, 1297, 1302 and 1317 mAh g^{-1}, respectively. The excess capacity to theoretic capacity of

Fe_2O_3 material is attributed to the irreversible capacity of decomposition of electrolyte to form a SEI layer. In the second cycle, the discharge capacities are 1098, 1150, 1107, and 1151 mAh g^{-1}. All the electrodes show good capacity retention at low current charge/discharge processes. The capacities of nanorods, nanotubes, nanodisks and nanorings Fe_2O_3 electrodes are 981, 1108, 1012 and 1106 mAh g^{-1}after 100 cycles, corresponding to capacity retentions of 89.3%, 96.3%, 91.4% and 96.2%. It is noticed that the capacities of nano-structured Fe_2O_3 materials are higher than the theoretic capacity of alpha-phase Fe_2O_3 while operating at low current, which can be ascribed to an interfacial lithium storage mechanism.[11] The similar trend of electrochemical performance at 0.1 C can be concluded from charge/discharge curves of 1st, 2nd and 100th cycles, as described in Figure S3. From the charge/discharge curves, we can also obtain the charge/discharge plateaus, which correspond to the redox peaks in CV measurements, as shown in Figure 3. High current testings were also carried out as shown in Figures 5 (b) and (c). All the cells were tested at 0.1 A g^{-1} for the first 3 cycles to activate electrode materials and then promoted to higher currents such as 1 and 10 A g^{-1}. In Figure 5(b), the nanotubes and nanorings present better electrochemical performance than their counterparts (nanorods and nanodisks) at the charge/discharge current of 1 A g^{-1}. The capacities of Fe_2O_3 nanotubes and nanorings after 100 cycles are 801 and 861 mAh g^{-1}, corresponding to capacity retentions of 94.2% and 94.7%. By contrast, the capacities of nanorods and nanodisks dramatically fade at the beginning and keep at a stable level after 50

Table 1. Physical properties and high rate electrochemical performance of Fe_2O_3 anode materials

Samples	Surface area (m^2/g)	Pore size distribution (nm)	Charge transfer resistance (Ohm)	Actviation Energy (kJ mol^{-1})	Rate performance (mAh g^{-1}, 10A g^{-1} after 1000 cycles)
nanorods	42.4	2.3	40.8	65.09	102
nanotubes	68.4	2.2	32.9	42.19	391
nanodisks	52.1	2.4	38.8	52.76	157
nanorings	89.6	2.5	30.5	22.19	447

cycles. The capacities of Fe_2O_3 nanorods and nanodisks are 574 and 683 mAh g^{-1}, corresponding to capacity retentions of 63.2% and 78.8%. At an extreme high charge/discharge current of 10 A g^{-1}, the nanotubes and nanorings electrodes still present excellent performance. Their capacities are 391 and 447 mAh g^{-1} after 1000 cycles, which are much higher than those of nanorods and nanodisks (102 and 157 mAh g^{-1}). The overall electrochemical performance of nanotubes and nanorings are superior to previous reports of alpha-phase with different morphologies.[9] The electrochemical enhancements of nanotubes and nanorings electrodes compared with their counterparts, especially in high rate performances, can be attributed to the benefits of the hollow structure. The higher surface area of nanotubes and nanorings can provide more active sites for lithium ion intercalation so that charges and electrons can go through electrode materials in short period. The lower dimensional size in nanotubes and nanorings ensure faster lithium ion diffusion kinetics. The intrinsic advantages such as lower charge transfer resistance and lower activation energy of hollow structured materials enhance the reactivity and intercalation dynamics.

In conclusion, two groups of nanostructured Fe_2O_3 materials with/without cavity (nanorods vs. nanotubes and nanodisks vs. nanorings) were prepared by a facile hydrothermal method. The physical properties and electrochemical performance of Fe_2O_3 anode materials are summarized in Table 1. Compared with their solid counterparts, the hollow structured materials (nanotubes and nanorings) have higher specific surface area, smaller dimensional size, lower charge transfer resistance and lower activation energy. These advantages are beneficial in enhancing the lithium diffusion dynamics, and hence, achieve excellent electrochemical performance for lithium ion batteries. The Fe_2O_3 nanotubes and nanorings exhibited higher specific capacities, better retentions and superior high rate performances, compared with their solid counterparts (nanorods and nanodisks). The Fe_2O_3 nanotubes and nanorings electrodes can achieve capacity of 391 and 447 mAh g^{-1} at a discharge current of 10 A g^{-1} after 1000 cycles. These results would be instructive for comparative studies of other nano-structured materials for lithium ion batteries.

Acknowledgement

GXW appreciates the support from ARC Future Fellow Project (FT1101100800). HL would like to thank the support from UTS Chancellor's Post Doctoral Fellowship (CPDF). The

authors acknowledge use of JEOL 2010 within the UoW Electron Microscopy Centre.

Notes and references

[a] *Centre for Clean Energy Technology, School of Chemistry and Forensic Science, Faculty of Science, University of Technology Sydney, Broadway Sydney, NSW 2007, Australia. E-mail: hao.liu@uts.edu.au; Guoxiu.Wang@uts.edu.au*

†Electronic Supplementary Information (ESI) available: [Details of experimental, X-ray diffraction patterns, N_2 adsorption results, charge/discharge curves]. See DOI: 10.1039/c000000x/

1 J. M. Tarascon and M. Armand, *Nature*, 2001, **414**, 359-367.

2 P. G. Bruce, B. Scrosati and J. M. Tarascon, *Angew. Chem. Int. Ed.*, 2008, **47**, 2930-2946.

3 (a) Y. Ren, Z. Ma, R. E. Morris, Z. Liu, F. Jiao, S. Dai and P. G. Bruce, *Nat. Commun.*, 2013, **4**, Article No. 2015; (b) F. Jiao, K. M. Shaju, and P. G. Bruce, *Angew. Chem. Int. Ed.*, 2005, **44**, 6550. (c) Y. Ren, L. J. Hardwick, and P. G. Bruce, *Angew. Chem. Int. Ed.*, 2010, **49**, 2570. (d) Y, Ren, A. R. Armstrong, F. Jiao and P. G. Bruce, *J. Am. Chem. Soc.*, 2010, **132**, 996. (e) F. Jiao and P. G. Bruce, *Adv. Mater.*, 2008, **19**, 657.

4 (a) J. Y. Luo, J. J. Zhang and Y. Y. Xia, *Chem. Mater.*, 2006, **18**, 5618; (b) H. Liu, G. X. Wang, J. Liu, S. Z. Qiao, and H. J. Ahn, *J. Mater. Chem.*, 2011, **21**, 3046. (c) H. S. Zhou, D. L. Li, M. Hibino and I. Honma, *Angew. Chem. Int. Ed.*, 2005, **44**, 797; (d) G. X. Wang, H. Liu, J. Horvat, B. Wang, S. Z. Qiao, J.S. Park and H. Ahn, *Chem. Eur. J.*, 2010, **16**, 11020. (e) Y. F. Shi, B. K. Guo, S. A. Corr, Q. H. Shi, Y. S. Hu, K. R. Heier, L. Q. Chen, R. Seshadri, and G. D. Stucky, *Nano Lett.*, 2010, **9**, 4215; (f) H. Liu, S, Chen, G. X. Wang and S. Z. Qiao, *Chem. Eur. J.*, 2013, **19**, 16897. (g) Y. Fang, Y. Y. Lv, R. C. Che, H. Y. Wu, X. H. Zhang, D. Gu, G. F. Zheng and D. Y. Zhao, *J. Am. Chem. Soc.*, 2013, **135**, 1524.

5 (a) X. W. Lou, C. Yuan, J. Y. Lee and L. A. Archer, *Adv. Mater.*, 2006, **18**, 2325; (b) Z. Y. Wang, D. Y. Luan, F. Y. C. Boey and X. W. Lou, *J. Am. Chem. Soc.*, 2011, **133**, 4738; (c) L. Zhou, D. Y. Zhao and X. W. Lou, *Angew. Chem. Int. Ed.*, 2012, **51**, 239; (d) Z. Y. Wang, L. Zhou and X. W. Lou, *Adv. Mater.*, 2012, **24**, 1903; (e) L. Zhou, D. Y. Zhao and X. W. Lou, *Adv. Mater.*, 2012, **24**, 745.

6 (a) J. Liu, S. Z. Qiao, J. S. Chen and X. W. Lou, *Chem. Commun.*, 2011, 47, 10443. (b) J. Liu, S. Z. Qiao, B. S. Hartono and G. Q. M. Lu, *Angew. Chem. Int. Ed.*, 2010, **49**, 4981-4985

7 Z. W. Seh, W. Y. Li, J. J. Cha, G. Y. Zheng, Y. Yang, M. T. McDowell, P. C. Hsu and Y. Cui, *Nat. Commun.* 2013, **4,** Article No. 1331.

8 (a) X. L. Hu, J. C. Yu, J. M. Gong, Q. Li, and G. S. Li, *Adv. Mater.*, 2007, **19**, 2324. (b) B. L. Lv, Y. Xu, D. Wu and Y. H. Sun, *CrystEngComm*, 2011, **13**, 7293.

9 (a) J. Chen, L. Xu, W. Li and X. L. Gou, *Adv. Mater.*, 2005, **17**, 582; (b) L. Chen, H. Y. Xu, L. E. Li, F. F. Wu, J. Yang and Y. T. Qian, *J. Power Sources* 2014, **245**, 429; (c) H. Liu, G. X. Wang, J. S. Park, J. Z. Wang, H. K. Liu and C. Zhang, *Electrochim. Acta* 2009, **54**, 1733.

10 (a) J. Chen and F. Y. Cheng, *Acc. Chem. Res.*, 2009, **42**, 713. (b) A. J. Bard and L. R. Faulkner, *Electrochemical Methods: Fundamentals and Applications*, 2nd ed., Wiley, New York, 2001.

11 J. Jamnik and J. Maier, *Phys. Chem. Chem. Phys.*, 2003, **5**, 5215.